

# A Source-Term Based Boundary Layer Bleed/Effusion Model for Passive Shock Control

R. A. Baurle and A. T. Norris  
Hypersonic Airbreathing Propulsion Branch  
NASA Langley Research Center  
Hampton, Va 23681

## ABSTRACT

A modeling framework for boundary layer effusion has been developed based on the use of source (or sink) terms instead of the usual practice of specifying bleed directly as a boundary condition. This framework allows the surface boundary condition (*i.e.* isothermal wall, adiabatic wall, slip wall, etc.) to remain unaltered in the presence of bleed. This approach also lends itself to easily permit the addition of empirical models for second-order effects that are not easily accounted for by simply defining “effective” transpiration values. Two effusion models formulated for supersonic flows have been implemented into this framework; the Dorer/Bohning law and the Slater formulation. These models were applied to unit problems that contain key aspects of the flow physics applicable to bleed systems designed for hypersonic air-breathing propulsion systems. The ability of each model to predict bulk bleed properties was assessed, as well as the response of the boundary layer as it passes through and downstream of the porous bleed system. The model assessment was performed with and without the presence of shock waves. Three-dimensional CFD simulations that included the geometric details of the porous plate were also carried out to supplement the experimental data, and provide additional insights into the bleed flow physics. Overall, both bleed formulations fared well for the tests performed in this study. However, the sample of test problems considered in this effort was not large enough to permit a comprehensive validation of the models.

## INTRODUCTION

The ability to control the boundary layer is an important issue for many aerospace applications, both subsonic and supersonic. Precise control can reduce the drag on a vehicle, alter the heat transfer characteristics of a surface, and improve the uniformity of the flow field. One of the main techniques used to control the boundary layer is the process of removing (or bleeding) the low-momentum flow at the solid surface. This has the effect of moving high-momentum flow closer to the surface, essentially thinning the boundary layer. This thinning can be especially important in the operation of supersonic engine inlets, where the physics of shock boundary layer interactions often dominate inlet and isolator performance.

In a typical ramjet or scramjet, the compression of the inlet air is not performed by mechanical means as is the case in a turbojet. Rather, the compression is accomplished by a shock system in the inlet and isolator sections of the engine. The design of the inlet and isolator components must contain and stabilize the shock system, but even small perturbations in the flow field can cause large-scale shock movements. If left uncontrolled, instabilities in the system can result in the shocks traveling upstream and out of the inlet,

---

<sup>†</sup> Approved for public release; distribution is unlimited.

causing an engine unstart. This phenomenon can lead to catastrophic results, including engine flame-out and structural damage. A common technique to control the positioning of the shocks in these systems is through passive control of the boundary layers.

The shock system in the isolator of a scramjet engine is characterized by low pressure on the upstream side and higher pressure downstream. The onset of the shock system is established by a balance between the flow momentum, driving the shock downstream of the inlet, and the strength of the combustion-induced pressure rise. The adverse pressure gradient associated with the shock system induces an aerodynamic contraction, due to a thickening (and local separation) of the isolator surface boundary layers. A mitigation of the aerodynamic contraction would allow the isolator to operate at lower flight Mach conditions, leading to a larger operability range for the vehicle. To control the thickness (and shape) of the boundary layer, the technique of boundary layer bleed can be employed. This is accomplished by having portions of the inlet and/or isolator walls composed of porous surfaces, backed by a plenum. By adjusting the plenum pressure to be less than the pressure at the surface, the low-momentum flow next to the surface is removed from the flow path, reducing the boundary layer thickness and improving the boundary layer shape factor. This reduces the aerodynamic contraction and improves the ability of the boundary layer to remain attached in the presence of shock/boundary layer interactions.

Unfortunately, accounting for bleed regions with Computational Fluid Dynamics (CFD) is not a trivial task. One of the characteristics of bleed regions is that the porous surfaces are often composed of many (on the order of hundreds or more) holes that have been drilled through the surface. These holes are small relative to the boundary layer thickness, and it is impracticable to resolve each discrete hole. To overcome this, models have been developed to account for the effects of bleed on the flow, without resorting to resolving all of the geometric details of the porous wall.

One of the simplest models is the Darcy Law, formulated by Bur. <sup>1</sup> This model essentially sets the velocity of the flow through the bleed holes to a value that is proportional to the pressure difference across the bleed surface,

$$u_h = \frac{\Phi d^2}{32 h \mu} (P_w - P_p) \quad (1)$$

where  $\Phi$  is the plate porosity,  $d$  is the hole diameter,  $h$  is the plate thickness,  $\mu$  is the molecular viscosity,  $P_w$  is the wall pressure, and  $P_p$  is the bleed system plenum pressure. Results obtained through the use of this model have been inconsistent. A more complex model is a formulation by Poll et al. <sup>2</sup> which is an empirical fit of data taken from many different bleed experiments. This model relates the mass flow rate ( $\dot{m}$ ) through the bleed holes to the pressure difference (normalized by  $\mu^2/d^2/\rho_h$ ) across the bleed surface,

$$\frac{\rho_h (P_w - P_p) d^2}{\mu^2} = \frac{h^2}{K d^2} \left[ 40.7 \left( \frac{\dot{m}}{\mu h} \right) + 1.95 \left( \frac{\dot{m}}{\mu h} \right)^2 \right] \quad (2)$$

While this model has experienced some success, the need to adjust the effective area constant,  $K$ , for each flow makes it a less attractive choice. Another approach that has been adopted is to simply assume that the flow is isentropic through the bleed orifices, allowing the relationship for the velocity in the bleed passages to be written as:

$$\frac{u_h^2}{2} = \frac{\gamma R T_p}{(\gamma - 1)} \left[ \left( \frac{P_w}{P_p} \right)^{\frac{\gamma-1}{\gamma}} - 1 \right] \quad (3)$$

However due to losses, a scaling factor has to be determined for each bleed case modeled.

The objective of this effort is to evaluate the performance of two promising boundary layer effusion models under conditions similar to what one might expect in the inlet or the isolator of a hypersonic propulsion system. The ability to model this phenomenon is particularly important for hypersonic propulsion systems, where long-duration ground testing is a difficult proposition. In fact, the degree to which computational modeling can be relied upon to optimize the performance and operability of hypersonic systems will likely determine the success of development efforts in this area. The two effusion models considered in this work are the formulations of Doerffer and Bohning <sup>3</sup> and Slater. <sup>4</sup> Both approaches employ an isentropic model

as the basis, and empirical relationships are introduced to account for the losses due to a non-ideal system. In addition, these models have been formulated with data from high-speed flows, and so are likely to be more applicable to hypersonic propulsion systems. The results of this effort will be used to determine the effectiveness of these models at predicting both the bulk bleed properties, and also the effect that the bleed system has on the flow field.

## EFFUSION MODEL FRAMEWORK

The common practice in effusion modeling<sup>3,4</sup> is to enforce bleed/effusion via the specification of a boundary condition. This strategy forces the dependent variables at all grid cell faces attached to the bleed surface to be set to some averaged state that matches the desired effusion flow rate. The specification of boundary layer effusion in this effort is accomplished through the introduction of source (or sink) terms in the grid cells adjacent to the bleed region of interest. The source terms account for the flux of mass, momentum, and energy of the fluid flow passing through the bleed passages, without requiring an averaging operator to relate the flux through the bleed orifice to an effective flux across the entire cell area. This approach allows the surface boundary condition (*i.e.* slip wall, isothermal wall, adiabatic wall, etc.) to remain unchanged in the presence of bleed, and is consistent with the observation that the porosity of practical bleed systems is relatively small (typically on the order of 20% or less). In other words, from a macroscopic viewpoint, the bleed region would appear as a solid surface. Another potential advantage of accounting for bleed via source terms is that it offers a direct path to add empirical models for turbulent (or viscous) effects.

The source terms added to the governing equations in this effort are expressed as follows:

$$\text{continuity} \quad \rightarrow \quad \dot{m}_h \cdot Y_h^m \quad (4a)$$

$$\text{momentum} \quad \rightarrow \quad \dot{m}_h \cdot u_h^i + A_h^i (P_h - P_w) \quad (4b)$$

$$\text{energy} \quad \rightarrow \quad \dot{m}_h \cdot H_h \quad (4c)$$

where:  $\dot{m}_h$  is the mass flow rate through the bleed holes associated with a given bleed cell interface,  $Y_h^m$  is the mass fraction of species “m” passing through the bleed holes, and  $(u_h^i, P_h, H_h)$  are the velocity components, pressure, and total enthalpy of the bleed hole fluid. The inclusion of the wall pressure ( $P_w$ ) in the source term for the momentum equations is meant to remove the flux contribution from the surface pressure acting on the portion of the surface occupied by the bleed orifices (erroneously introduced when evaluating the inviscid fluxes). Two different effusion formulations have been considered in this effort to determine the bleed hole properties ( $\dot{m}_h, Y_h^m, u_h^i, P_h,$  and  $H_h$ ). One formulation is due to Doerffer and Bohning<sup>3</sup>, and the other is a formulation due to Slater.<sup>4</sup>

### Doerffer/Bohning Model

The bleed model of Doerffer and Bohning<sup>3</sup> is described by the following expressions (see Fig. 1 for a pictorial representation):

$$\text{If } (P_p \geq P_w) : \quad P_p - P_w = P_p \left[ \frac{M_h}{1.2} \right]^{0.55} \quad (5a)$$

$$\text{If } (P_w > P_p) : \quad P_w - P_p = P_w \left[ \left( \frac{M_h}{1.2} \right)^{0.55} + 25 M_h^{0.55} (C_{f,h} M_h)^{\frac{1}{1.52}} \right] \quad (5b)$$

This equation defines the relation between the pressure drop across the porous plate and the effective Mach number of the flow through the bleed orifices. The functional form of the Doerffer/Bohning effusion model depends on the magnitude of the plenum pressure relative to the wall pressure. When the plenum

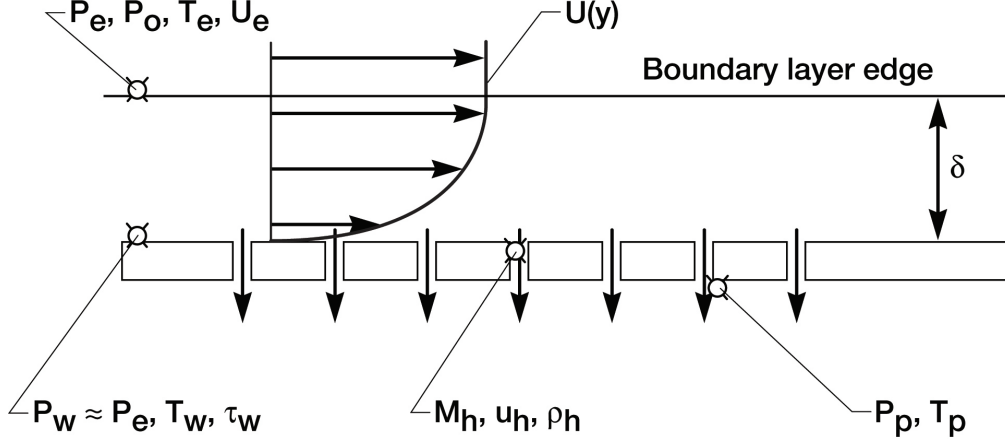


Figure 1: Schematic of effusion through a porous plate

pressure is greater than the local wall pressure (Eq. 5a), the flow is drawn out of the bleed plenum and into the boundary layer. Boundary layer bleed, on the other hand, results when the local surface pressure exceeds the plenum pressure (Eq. 5b). Doerffer and Bohning found a “blockage” effect when bleeding flow from the boundary layer into the plenum that was not present when flow effused from the plenum into the boundary layer. They theorized that the “blockage” effect was the result of the shear force present at the entrance of the bleed orifices. To account for this effect, a term that depends on the surface shear stress (normalized by the dynamic pressure of the bleed orifice)

$$C_{f,h} \equiv \frac{\tau_w}{\frac{\rho_h u_h^2}{2}} = \frac{2\tau_w}{\gamma P_h M_h^2} = \frac{2\tau_w \left(1 + \frac{\gamma-1}{2} M_h^2\right)^{\frac{\gamma}{\gamma-1}}}{\gamma P_w M_h^2}, \quad (6)$$

was added to the formulation. Equations 5a, 5b, and 6 reveal that the effective hole Mach number ( $M_h$ ), is solely a function of the plenum pressure ( $P_p$ ), surface pressure ( $P_w$ ), and the surface shear stress ( $\tau_w$ ). It should be noted that the surface shear stress included in this formulation is intended to be the value associated with the approach flow upstream of the porous plate.

The mass flow rate through the bleed orifices of a given cell interface can be expressed as follows:

$$\dot{m}_h = P_o \Phi_{aero} A_{cell} M_h \left(\frac{\gamma}{RT_o}\right)^{\frac{1}{2}} \left(1 + \frac{\gamma-1}{2} M_h^2\right)^{\frac{\gamma+1}{2(\gamma-1)}} \quad (7)$$

where  $P_o$  and  $T_o$  are either taken as the wall pressure and temperature (if  $P_w > P_p$ ), or the plenum pressure and temperature (if  $P_p \geq P_w$ ). An important aspect of this effusion model is the “aerodynamic” porosity ( $\Phi_{aero}$ ) that appears in Eq. 7. Doerffer and Bohning performed static transpiration tests on 22 different porous plates with geometrical porosities ranging from 2% to 26.6%, and found that bleed plates with identical geometrical porosities can result in quite different “aerodynamic” porosities. Hence, the length to diameter ratio as well as the quality of the drilled holes must be accounted for. Based on the 22 plates tested in Ref 3, the following empirical fit to the data was formulated:

$$\frac{P_w - P_p}{P_w} = 0.063 \left(\frac{\dot{m}}{A_{aero}}\right)^2 \quad (8)$$

which relates the “aerodynamic” hole area to the normalized pressure drop across the porous plate and the total effused flow rate. The “aerodynamic” porosity is then obtained by dividing  $A_{aero}$  by the total porous plate area. The above formula (Eq. 8) assumes that the static transpiration test involved the bleeding of air into the plenum (as shown in Fig. 1). The plenum and wall pressures would be swapped in Eq. 8 for static tests that instead effused air from of the plenum.

The implementation of the Doerffer/Bohning model in the present computational framework is as follows:

- At a given surface cell interface, Eq. 5a (or 5b) is evaluated to determine the effective hole Mach number given the surface pressure, bleed plenum pressure, and surface shear stress (if  $P_w > P_p$ ).
- The remaining bleed hole properties are evaluated given  $M_h$  and either  $P_w$  and  $T_w$  (if  $P_w > P_p$ ), or  $P_p$  and  $T_p$  (if  $P_p \geq P_w$ ).
- Eq. 7 is evaluated to obtain the local effusion rate at the surface cell interface given  $P_o$ ,  $T_o$ ,  $M_h$ , and  $A_{aero}$  (either estimated or obtained from static porous plate tests).
- The porous plate hole properties together with  $\dot{m}_h$  are then used to evaluate the effusion source terms.

### Slater Model

The bleed model developed by Slater <sup>4</sup> is based on a parametrization of the bleed physics that uses the concept of the sonic flow coefficient ( $Q_{sonic}$ ), defined via the relation:

$$\dot{m}_{bleed} = Q_{sonic} \dot{m}_{sonic} \quad (9)$$

$Q_{sonic}$  is a parameter that essentially measures the effectiveness of the bleed process, and its value must be obtained from some external means (*e.g.* measurements). A sample set of  $Q_{sonic}$  values derived from measurements <sup>5</sup> at four Mach number conditions is given in Fig. 2. For a calorically perfect gas, the mass flow rate ( $\dot{m}$ ) can be expressed as

$$\dot{m} = P_o \Phi A_{cell} M \left( \frac{\gamma}{RT_o} \right)^{\frac{1}{2}} \left( 1 + \frac{\gamma - 1}{2} M^2 \right)^{\frac{\gamma + 1}{2(1 - \gamma)}} \quad (10)$$

The reference bleed flow rate ( $\dot{m}_{sonic}$ ), defined as an isentropic sonic flow condition through the bleed holes, is obtained from this expression by setting the Mach number to one, *i.e.*

$$\dot{m}_{sonic} = P_o \Phi A_{cell} \left( \frac{\gamma}{RT_o} \right)^{\frac{1}{2}} \left( \frac{\gamma + 1}{2} \right)^{\frac{\gamma + 1}{2(1 - \gamma)}} \quad (11)$$

Earlier versions of bleed models based on this framework evaluated  $\dot{m}_{sonic}$  using boundary layer edge values for total pressure ( $P_o$ ) and total temperature ( $T_o$ ), along with a table look-up procedure to extract measured  $Q_{sonic}$  values (from curves similar to that given in Fig. 2) given the bleed plenum pressure and boundary layer edge values for Mach number and total pressure. However, the extraction of boundary layer edge conditions is at best a cumbersome process for a CFD solver, and at worst may not be well-defined depending on the complexity of the flow field. The Slater model addresses this issue by introducing a different reference value for  $\dot{m}_{bleed}$  that is based on surface properties rather than boundary layer edge conditions, *i.e.*

$$\dot{m}_{sonic}^* = P_w \Phi A_{cell} \left( \frac{\gamma}{RT_w} \right)^{\frac{1}{2}} \left( \frac{\gamma + 1}{2} \right)^{\frac{\gamma + 1}{2(1 - \gamma)}} \quad (12)$$

A surface sonic flow coefficient is also defined in a manner analogous to Eq. 9:

$$\dot{m}_{bleed} = Q_{sonic}^* \dot{m}_{sonic}^* \quad (13)$$

An evaluation of Eqs. 9, 11, 12, and 13 shows that  $Q_{sonic}^*$  is related to  $Q_{sonic}$  via the expression

$$Q_{sonic}^* = Q_{sonic} \left( \frac{P_o}{P_w} \right) \left( \frac{T_w}{T_o} \right)^{\frac{1}{2}} \quad (14)$$

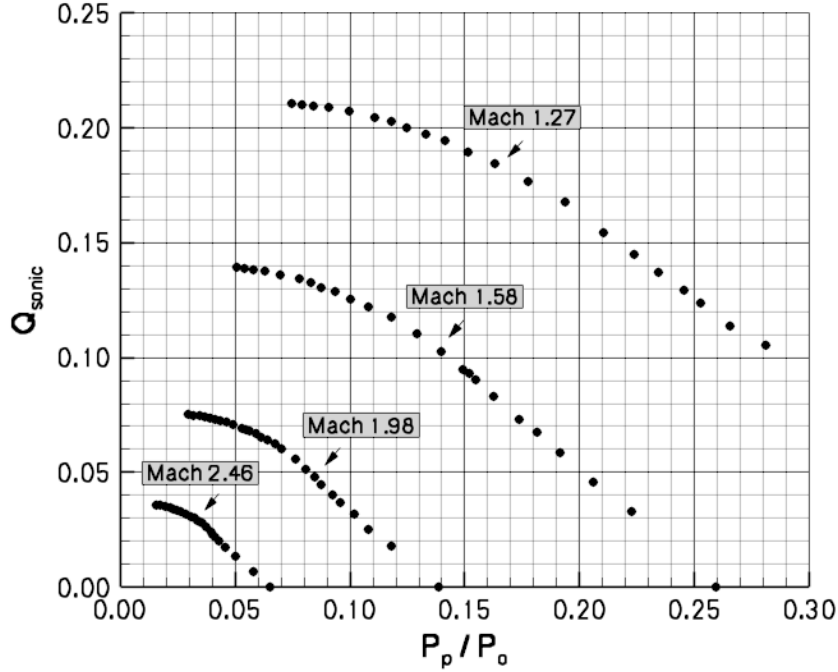


Figure 2: Sonic coefficient data plotted against plenum to total pressure ratio

To simplify the scaling, Slater assumed that the edge pressure is imposed through the boundary layer (standard boundary layer approximation) along with the assumption of a near-unity temperature recovery factor, *i.e.*

$$\frac{P_o}{P_w} \approx \frac{P_o}{P_e} = \left(1 + \frac{\gamma - 1}{2} M_e^2\right)^{\frac{\gamma}{\gamma - 1}} \quad (15a)$$

$$\frac{T_w}{T_o} \approx 1.0 \quad (15b)$$

With this simplification, the final scaling of  $Q_{sonic}$  and  $\frac{P_p}{P_o}$  (*i.e.* the independent and dependent variables in Fig. 2) are as follows:

$$Q_{sonic}^* = Q_{sonic} \left(\frac{P_o}{P_w}\right) \quad (16a)$$

$$\frac{P_p}{P_w} = \frac{P_p}{P_o} \left(\frac{P_o}{P_w}\right) \quad (16b)$$

The above scaling results in the surface sonic flow coefficient data shown in Fig. 3. This scaling collapses the separate curves in Fig. 2 for each Mach number, effectively removing Mach number from the parametrization. Slater fit the following quadratic curve to the data presented in Fig. 3:

$$Q_{sonic}^* = 0.59799735 + 0.03069346 \left(\frac{P_p}{P_w}\right) - 0.59361420 \left(\frac{P_p}{P_w}\right)^2 \quad (17)$$

The implementation of the Slater model in the present computational framework is as follows:

- Eq. 17 is evaluated to obtain  $Q_{sonic}^*$  at the surface cell interface given the surface pressure and the bleed plenum pressure.

- Eq. 12 is evaluated to obtain  $\dot{m}_{sonic}$  at the surface cell interface given the surface pressure and temperature.
- Eq. 13 is evaluated to determine the  $\dot{m}_{bleed} = \dot{m}_h$  required to evaluate the effusion source terms.
- Eq. 10 is used to determine the effective Mach number in the bleed holes ( $M = M_h$ ):
  - If  $Q_{sonic}^*$  is positive (*i.e.* flow is drawn into the plenum), then Eq. 10 is evaluated with  $P_o = P_w$  and  $T_o = T_w$ .
  - If  $Q_{sonic}^*$  is negative (*i.e.* flow is drawn out of the plenum), then Eq. 10 is evaluated with  $P_o = P_p$  and  $T_o = T_p$ .
- The remaining bleed hole properties are evaluated given  $P_o$ ,  $T_o$ , and  $M_h$ .

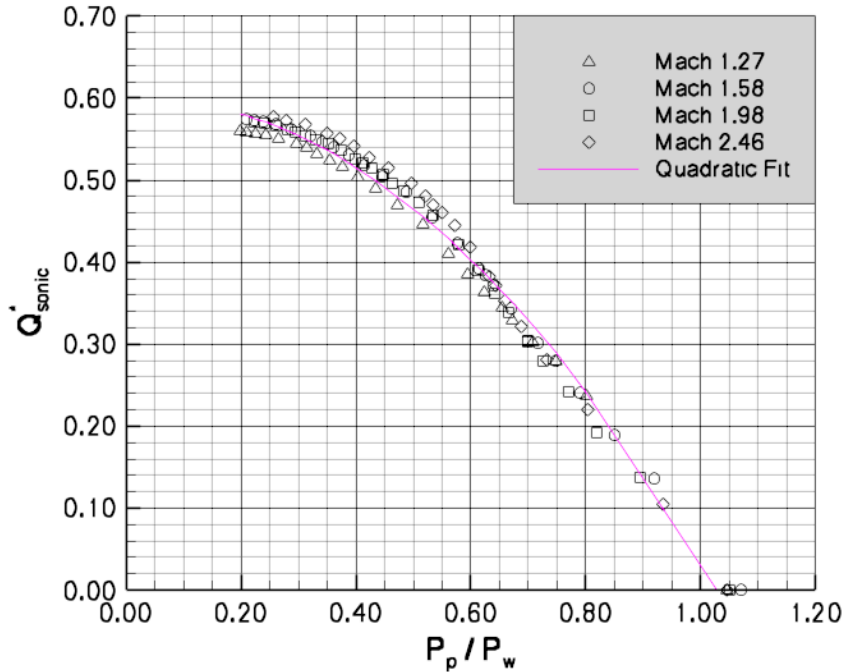


Figure 3: Surface sonic coefficient data plotted against plenum to surface pressure ratio

### Plenum Properties

The final aspect of the effusion model framework is the inclusion of a plenum (modeled as a control volume) to balance the flow rates entering (or exiting) the computational domain with those exiting (or entering) from some external source. The process is schematically shown in Fig. 4.

The plenum properties, which are required for both effusion models described above, are determined by considering the balance of flow rates entering and exiting the plenum:

$$\frac{d}{dt}(\rho_p) = \frac{1}{Vol} \left( \dot{m}_{bleed} + \sum_{n=1}^{n_{cells}} \dot{m}_h \right) \quad (18)$$

where  $n_{cells}$  is the number of grid cells in the computational domain that interfaces with the plenum,  $\rho_p$  is the plenum fluid density,  $Vol$  is the plenum volume, and  $\dot{m}_{bleed}$  is the specified effusion flow rate exiting (or entering) the plenum. The sign convention for the mass flow rates is positive for flow exiting the plenum

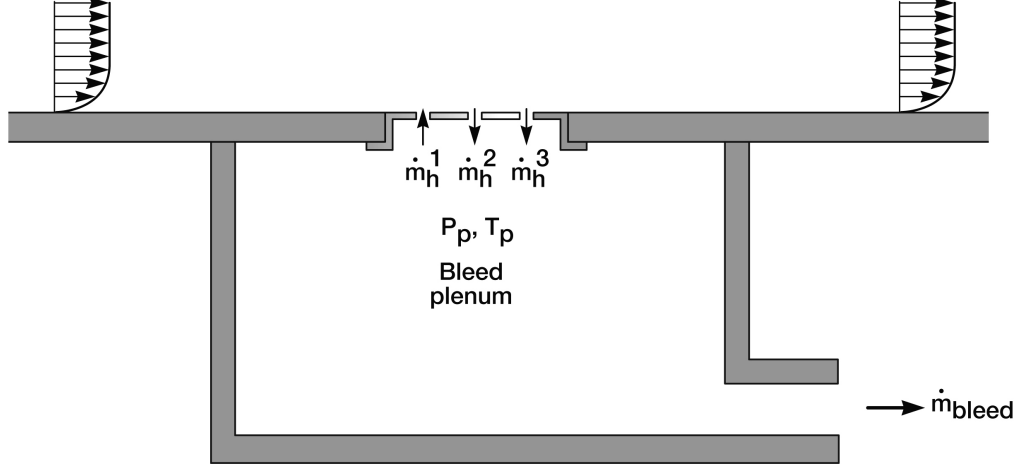


Figure 4: Schematic of effusion process including the plenum (modeled as a control volume)

and negative for flow entering the plenum. In a similar fashion, the energy ( $E_p$ ) and composition ( $Y_p^m$ ) of the plenum gas are determined from the following relationships:

$$\frac{d}{dt}(\rho_p E_p) = \frac{1}{Vol} \left( \dot{m}_{bleed} \cdot H + \sum_{n=1}^{n_{cells}} \dot{m}_h \cdot H_h \right) \quad (19)$$

$$\frac{d}{dt}(\rho_p Y_p^m) = \frac{1}{Vol} \left( \dot{m}_{bleed} \cdot Y^m + \sum_{n=1}^{n_{cells}} \dot{m}_h \cdot Y_h^m \right) \quad (20)$$

The values for  $H$  and  $Y^m$  are simply the current plenum values if flow is drawn out of the plenum (*i.e.*  $\dot{m}_{bleed} \geq 0$ ). If flow is supplied to the plenum ( $\dot{m}_{bleed} < 0$ ), the values for  $H$  and  $Y^m$  must be specified. The integration of Eqs. 18, 19, and 20 are sufficient to describe the thermodynamic state of the plenum. However, for the steady-state simulations considered in this effort, the resulting plenum pressure was under-relaxed to improve the robustness of the solution procedure, *i.e.*

$$P_p^{new} = r P_p^{new} + (1 - r) P_p^{old}, \quad (0 < r \leq 1) \quad (21)$$

where  $r$  is the chosen relaxation parameter.

## RESULTS AND DISCUSSION

Two similar porous flat plate bleed configurations were chosen to evaluate the performance of the two effusion models considered in this effort. The first configuration involved flow over a porous flat plate at Mach numbers of 1.58, 1.98, and 2.46. A variety of bleed flow rates were simulated for this configuration to determine the ability of each model to predict the bulk bleed flow properties, as well as the response of the boundary layer as it passes through and downstream of the bleed system. The second configuration considered the more difficult scenario of a Mach 2.46 oblique shock wave interacting with a porous plate bleed system. Three-dimensional CFD simulations, that included the geometric details of the bleed system, were also carried out for this configuration. The analysis of the simulations for this configuration focused on the ability of each effusion model to predict the bleed behavior in the presence of a strong adverse pressure gradient. Parameters of interest included the reduction in flow separation and the recovery rate of the boundary layer. The assessment of the models was accomplished through comparisons made with the measurements and the three-dimensional CFD results.

All computational results were obtained using the VULCAN (Viscous Upwind aLgorithm for Complex flow ANalysis) Navier-Stokes code. <sup>6</sup> The CFD data were acquired by integrating the Reynolds-Averaged Navier-Stokes equations until steady-state conditions were achieved. All of the solutions were advanced in pseudo-time with an Incomplete LU factorization scheme using a Courant-Friedrichs-Lewy (CFL) number in the range of 25 -  $10^6$ . The inviscid fluxes were evaluated by using the Low-Diffusion Flux Split Scheme (LDFSS) of Edwards, <sup>7</sup> with interface variable reconstruction achieved via the  $\kappa = 1/3$  Monotone Upstream-centered Scheme for Conservation Laws (MUSCL). The van Leer limiter <sup>8</sup> was also included to avoid spurious oscillations during the reconstruction process. The viscous fluxes were evaluated using standard  $2^{nd}$ -order accurate central differences. The Menter shear-stress-transport (Menter-SST)  $k-\omega$  turbulence model <sup>9</sup> was used for all simulations, with the the turbulent Prandtl number set to 0.9.

### Uniform Supersonic Flow Porous Plate Flow

The first configuration considered was a uniform supersonic flow (Mach 1.58, 1.98, and 2.46) over a porous flat plate. The porous plate simulated was the C1 plate taken from Willis et al. <sup>5</sup> This configuration (see Fig. 5) has 75 circular 90° bleed holes (that are open to the bleed plenum) distributed over a 2.75 by 7.0 inch area. The bleed plate is 0.25 inches thick, and each bleed orifice has a diameter of 0.25 inches. The resulting geometric porosity of the plate is 0.19. Static tests were not reported on this bleed system, so the value of  $A_{aero}$  (required for the Doerffer/Bohning effusion model) had to be estimated. Based on the fact that the bleed holes are relatively large with a length to depth ratio of unity, and given that the bleed holes have no noticeable geometric flaws (see Fig. 5), the aerodynamic porosity was simply assumed to be equal to the geometric porosity. The porous plate was mounted flush to the  $1 \times 1$  Supersonic Wind Tunnel (SWT) test section sidewall, so the approach boundary layer is that of the naturally occurring facility boundary layer. Boundary layer fences were placed on each side of the porous plate to isolate the region of interest from any facility corner flow effects. Hence, the flow is expected to be reasonably approximated as a two-dimensional configuration. The facility flow conditions and boundary layer characteristics at the reference plane (3.225 inches upstream of the bleed region) are given in Table 1. The approach flow conditions at the reference plane were measured using a translating pitot probe and wall static pressure taps. The uncertainty in the measurements was reported as 0.007 psi for static pressure, 0.045 psi for pitot pressure, and 2.4% (relative to the measured value) for  $Q_{sonic}$ . Further details on the experimental set up, measurement techniques, and uncertainty analysis are given in Ref. 5.

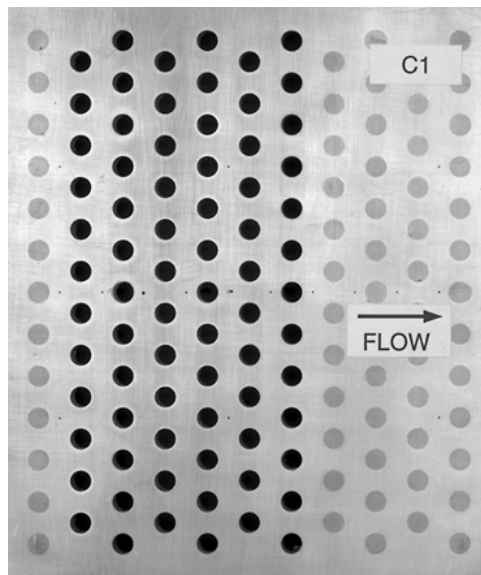


Figure 5: Photograph of the C1 plate ( $\Phi = 0.19$ )

Table 1: Porous Plate 1 × 1 SWT Test Conditions

|                       | Mach 1.58     | Mach 1.98     | Mach 2.46     |
|-----------------------|---------------|---------------|---------------|
| Total Pressure [kPa]  | 103.4         | 137.9         | 172.4         |
| Total Temperature [K] | 293.0         | 293.0         | 293.0         |
| $\delta$ [cm]         | 2.10          | 2.44          | 2.63          |
| $\delta^*$ [cm]       | 0.436 (0.459) | 0.567 (0.600) | 0.717 (0.784) |
| $\theta$ [cm]         | 0.192 (0.192) | 0.202 (0.199) | 0.198 (0.198) |
| $C_f \times 10^3$     | 1.69 (1.72)   | 1.50 (1.52)   | 1.29 (1.36)   |

Mach number and boundary layer properties measured at the reference plane  
 Boundary layer properties in parentheses are computed flat plate CFD values

The CFD simulations for this configuration were performed on a two-dimensional domain that extended from the reference plane (3.225 inches upstream of the bleed region) up to a streamwise station 4.25 inches downstream of the bleed region (see Fig. 6). The facility walls, including the bleed region, were specified as a no-slip adiabatic condition. The coordinates of the facility nozzles were not available, so the inflow (reference plane) conditions were set using variable profiles extracted from separate flat plate simulations that were performed to allow the boundary layers to develop until the measured integral properties were nominally matched. The boundary layer properties extracted from these profiles are listed in parentheses along side of the measured values in Table 1. The momentum thickness ( $\theta$ ) was the parameter that was matched when choosing the reference plane to extract from the flat plate solutions. The resulting percent differences in displacement thickness ( $\delta^*$ ) were 5.3%, 5.8%, and 9.3% for the Mach 1.58, 1.98, and 2.46 conditions, respectively. Similarly, the percent differences in skin friction coefficient ( $C_f$ ) were 1.8%, 1.3%, and 5.4%. All flow properties were extrapolated at the outflow and farfield boundaries.

The grid generated for this geometry was crafted based on information extracted from a detailed grid resolution study performed in Ref. 4, using a numerical scheme similar to that employed in this effort. The wall-normal grid spacing was set to  $1.0 \times 10^{-4}$  inches, which resulted in nominal  $y^+$  values of 0.35, 0.30, and 0.21 for the Mach 1.58, 1.98, and 2.46 conditions, respectively. The grid was stretched at a rate of 3% (or less) through the extent of the boundary layer. A total of 100 cells were evenly distributed axially over the bleed region, yielding a streamwise spacing of 0.0275 inches. This spacing corresponds to approximately 10 cells per bleed orifice diameter. The total grid size was  $201 \times 225$ .

The effect of boundary layer bleed on the bulk flow properties is illustrated in Figs. 7 and 8. These images show contours of Mach number overlaid with the wall-normal component of the velocity vectors adjacent to the bleed region. The bleed mass flow rate was 0.4 kg/s, which is close to the value that would choke the bleed orifices. The results obtained from the use of the Doerffer/Bohning model are shown in Fig. 7, while Fig. 8 displays results obtained from the Slater model. Both images are qualitatively similar, with a fairly uniform bleed flow rate across the full extent of the bleed region. The suction of boundary layer fluid results in an expansion fan at the start of the bleed region, followed by a recompression at the exit of the porous region. The Mach number remains fairly constant in the core flow above the bleed region, but is somewhat larger than the approach flow due to the localized expansion that results as the flow is bled out of the domain.

Although the overall flow properties showed very little differences between the two bleed formulations, differences are evident when specific bleed parameters are compared. Figure 9 compares the  $Q_{sonic}$  values computed from Eqs. 9 and 11. The Doerffer/Bohning formulation does a reasonable job of predicting the measured values, particularly at the larger Mach number conditions. In general, this formulation tends to underpredict the  $Q_{sonic}$  values for low bleed flow rates (large  $P_p/P_o$ ), while the values are overpredicted for bleed rates that approach the choking limit of the porous plate (*i.e.*  $P_p \Rightarrow 0$ ). The Slater formulation, on the other hand, consistently underpredicts the  $Q_{sonic}$  values for all Mach conditions. At first glance, one may not expect this result given the fact that this particular model was calibrated using the experimental data shown in these comparisons. A close examination of the assumptions made in the development of the model,

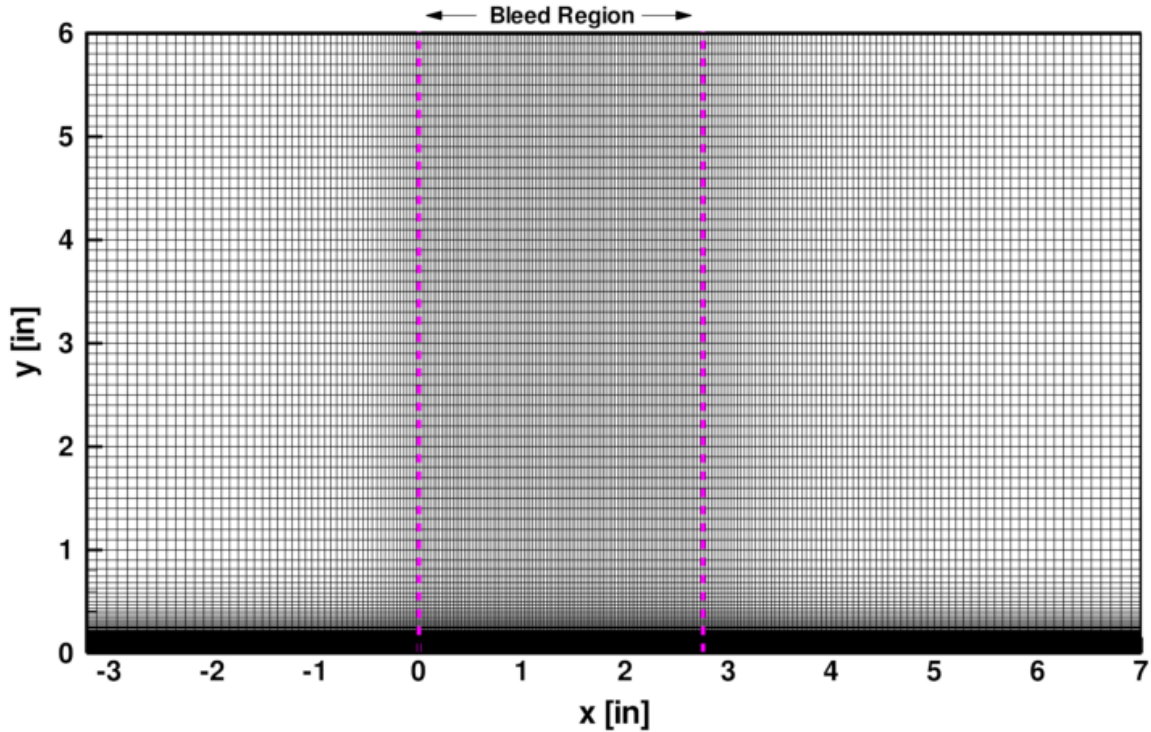


Figure 6: Solution domain for the C1 porous plate simulations (bleed region bounded by purple lines)

however, reveals the reason for the consistent underprediction of the  $Q_{sonic}$  values. In order to remove the dependence on the boundary layer edge properties from earlier versions of this model, it was assumed that the wall pressure was approximately equal to the boundary layer edge pressure (see Eq. 15a). This assumption allows  $P_o/P_w$  to be written in terms of the boundary layer edge Mach number ( $M_e$ ). In general, this assumption is a reasonable one, provided that  $M_e$  is known. However, as shown in Figs. 7 and 8, there is a local expansion present over the bleed region. Hence, the edge Mach number in this region is a value somewhat larger than the facility Mach number. The wall pressure in the CFD simulation includes the effect of this local expansion, resulting in a larger value for  $P_o/P_w$ . Therefore, Eq. 16a would predict a lower value for  $Q_{sonic}$ , given the curve fit value for  $Q_{sonic}^*$  (Eq. 17). A confirmation of this observation is achieved if one repeats the Slater model simulations with the local wall pressure hard-coded to the unperturbed approach flow value (in effect forcing the model to use the upstream value for  $M_e$ ). Fig. 10 shows that the results from this exercise yields a very close fit to the experimental values.

One of the benefits of introducing a boundary layer bleed system is to control the thickness (and shape) of the boundary layer. Bleeding off the low-momentum flow of the inner portion of the boundary layer profile reduces the boundary layer thickness and improves the ability of the boundary layer to remain attached in the presence of adverse pressure gradients (*e.g.* shock boundary layer interactions). Hence, the ability of a bleed model to predict the boundary layer shape adjustments caused by the bleed system is an important factor to consider. A follow-on experimental effort<sup>10</sup> was undertaken to perform boundary layer pitot pressure surveys downstream of the same bleed systems considered in Ref. 5. The tunnel conditions were nominally the same as those given in Table 1. The pitot pressure surveys were measured using a translating pitot probe. Further details on the experimental set up, measurement techniques, and uncertainty analysis are given in Refs. 5 and 10.

A comparison of the boundary layer pitot pressure profiles with measurements are shown in Figs. 11, 12, and 13. The images are arranged from left to right to show the effect that increasing the bleed mass flow rate has on the boundary layer profiles. The left image in each of these figures contains the pitot profiles that

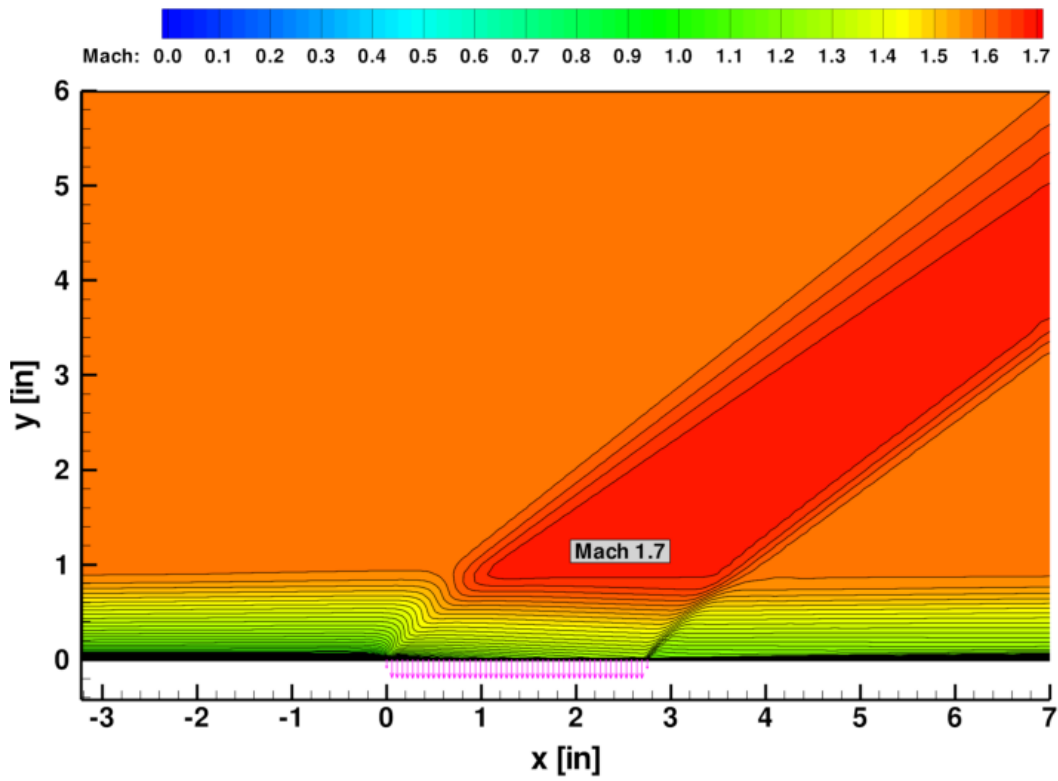


Figure 7: Mach contours for Mach 1.58 flow over the C1 porous plate (Doerffer/Bohning,  $\dot{m}_{bleed} = 0.4$  kg/s)

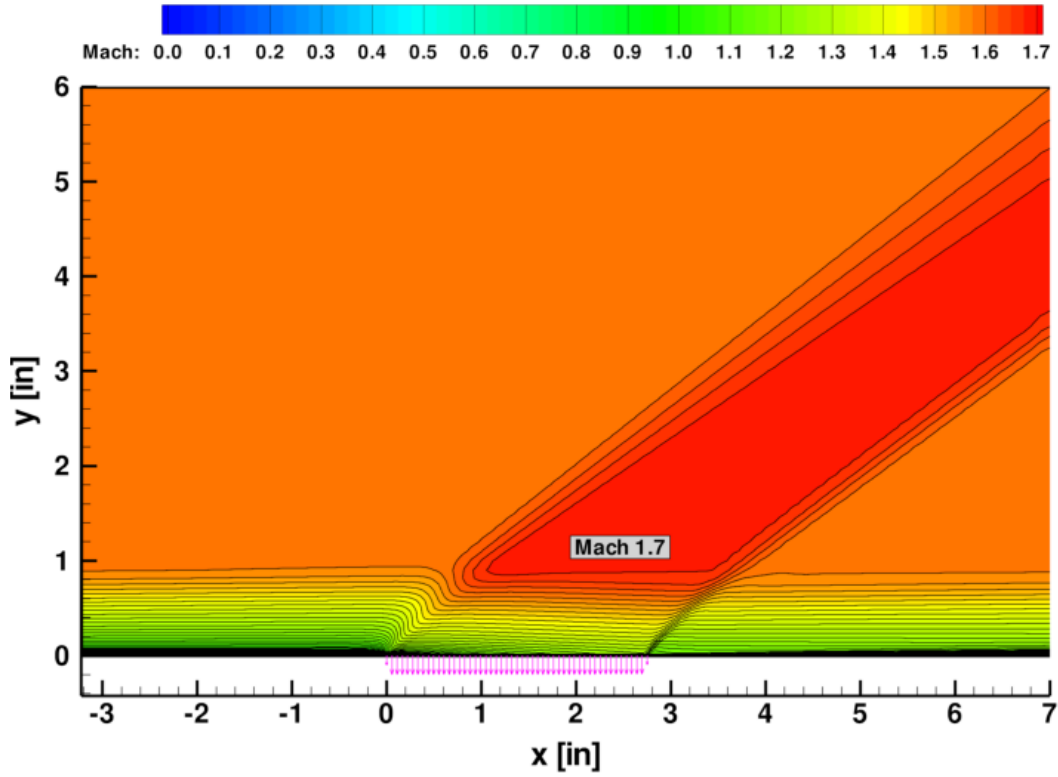


Figure 8: Mach contours for Mach 1.58 flow over the C1 porous plate (Slater,  $\dot{m}_{bleed} = 0.4$  kg/s)

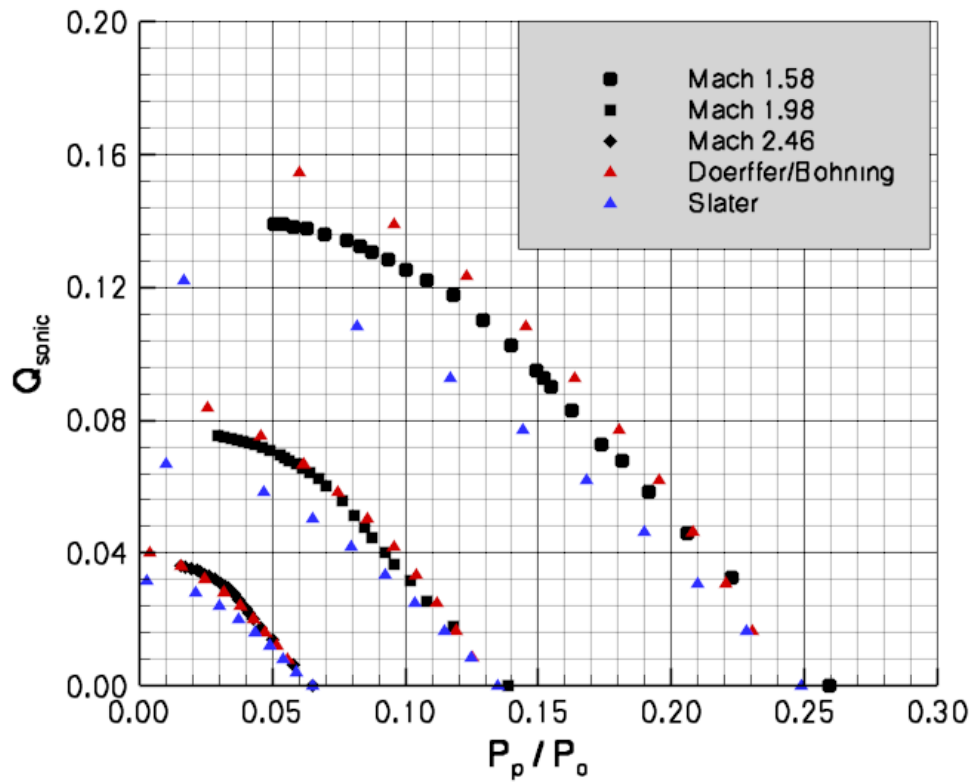


Figure 9: Comparison of sonic coefficient data plotted against plenum to total pressure ratio

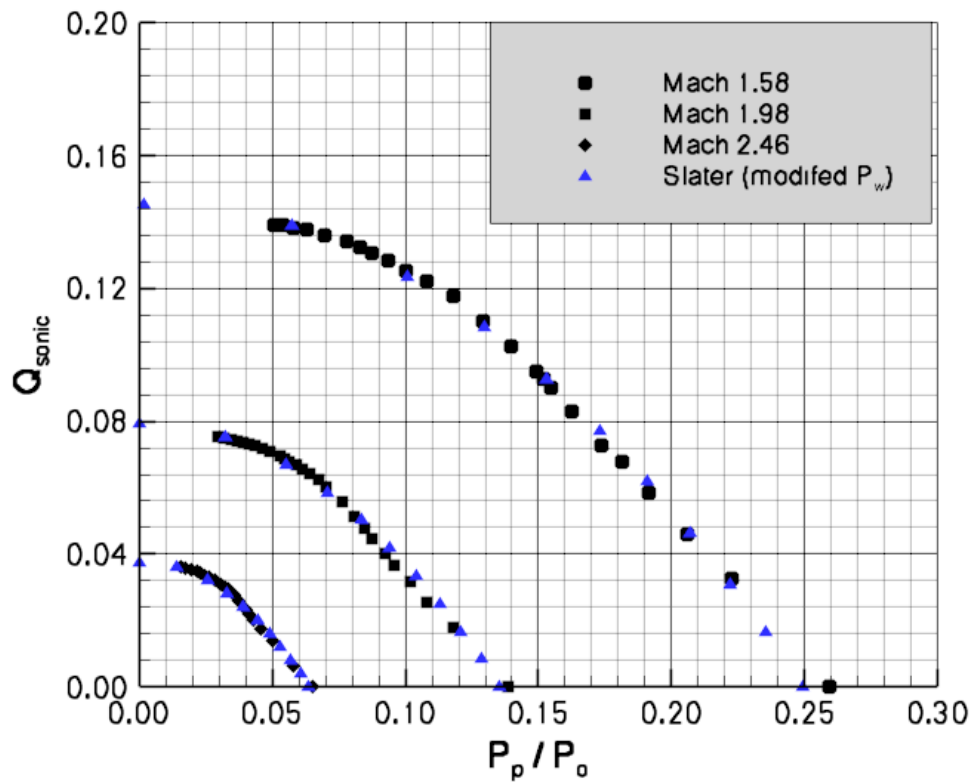


Figure 10: Comparison of sonic coefficient data when  $P_w$  is set to the approach flow value

result from the natural boundary layer growth along the facility sidewall. The images on the right correspond to a bleed mass flow rate that is near the choking limit of the bleed system. The center images represent a bleed mass flow rate that is roughly half the value required to choke the bleed orifices. Focusing first on the zero net bleed rate conditions, the computed pitot profiles for all three Mach numbers are somewhat fuller near the surface than what is indicated in the measurements. This is due in part to the “surface roughness effect” that exists as the flow negotiates around the bleed holes (measurements taken with the bleed orifices filled in have confirmed this effect). Global bleed models are really not designed to capture the physics associated with this phenomenon. Another contributing factor could be the fact that the measured boundary layer profiles were formed in the presence of a favorable pressure gradient through the facility nozzles, whereas the boundary layer development in the simulations took place in a zero pressure gradient environment. As the bleed flow rate is increased, both bleed models do a reasonable job at predicting the relative adjustments in the boundary layer profile. The profiles with boundary layer bleed are also too “full” near the surface, but this may simply be due to the fact that the computed approach flow had the same flaw. It should be noted that the measured Mach 1.98 pitot pressure profiles with non-zero bleed rates appear to have some systematic issue associated with them. At least it is not clear at this point why the core flow pitot pressure should increase in the presence of bleed. If one ignores this discrepancy, the overall agreement indicated by both bleed models with the measurements is reasonable.

### Oblique Shock / Porous Plate Interaction Flow

The second configuration involves a more complicated scenario of an oblique shock impinging on a modified version of the C1 plate described in the previous section. A schematic of the experimental set up is shown in Fig. 14. The modified porous plate has 2 extra rows of bleed holes opened up to the plenum, resulting in a total of 100 circular 90° bleed holes distributed over a 3.75 by 6.25 inch area. The bleed plate is 0.25 inches thick, and each bleed orifice has a diameter of 0.25 inches. The geometric porosity of the bleed plate is 0.21. The porous plate was mounted flush to the 1 × 1 Supersonic Wind Tunnel (SWT) test section sidewall. The shock generator was installed at a deflection angle of 8°, which was found to be sufficient to separate the boundary layer on the facility wall. The shock generator was positioned such that the oblique shock impinges at the mid-point of the bleed region based on inviscid flow theory. The shock generator spans the entire width of the wind tunnel, so boundary layer fences were placed on either side of the porous plate to isolate the region of interest from interactions between the shock wave and the facility corner flows. The facility flow conditions and boundary layer characteristics at the reference plane (3.225 inches upstream of the bleed region) are given in Table 2. The approach flow conditions at the reference plane were measured using a translating pitot probe and wall static pressure taps. The uncertainty in the measurements was reported as 0.007 psi for static pressure and 0.021 psi for pitot pressure. Further details on the experimental set up and the measurement techniques are given in Ref. 11.

Table 2: Oblique shock / Porous Plate 1 × 1 SWT Test Conditions

|                                 |               |
|---------------------------------|---------------|
| Mach                            | 2.46          |
| Total Pressure [kPa]            | 172.4         |
| Total Temperature [K]           | 293.0         |
| Choked $\dot{m}_{bleed}$ [kg/s] | 0.0885        |
| $\delta$ [cm]                   | 2.63          |
| $\delta^*$ [cm]                 | 0.727 (0.775) |
| $\theta$ [cm]                   | 0.196 (0.196) |
| $C_f \times 10^3$               | 1.43 (1.36)   |

Mach number and boundary layer properties measured at the reference plane  
Boundary layer properties in parentheses are computed flat plate CFD values

Both three-dimensional and two-dimensional CFD simulations were performed for this configuration. The

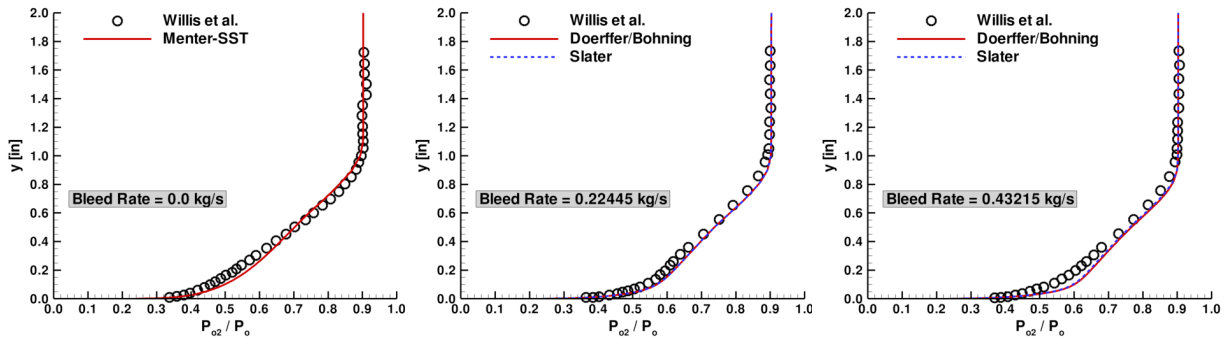


Figure 11: Boundary layer pitot pressure surveys 3.5 inches downstream of the bleed plate (Mach 1.58)

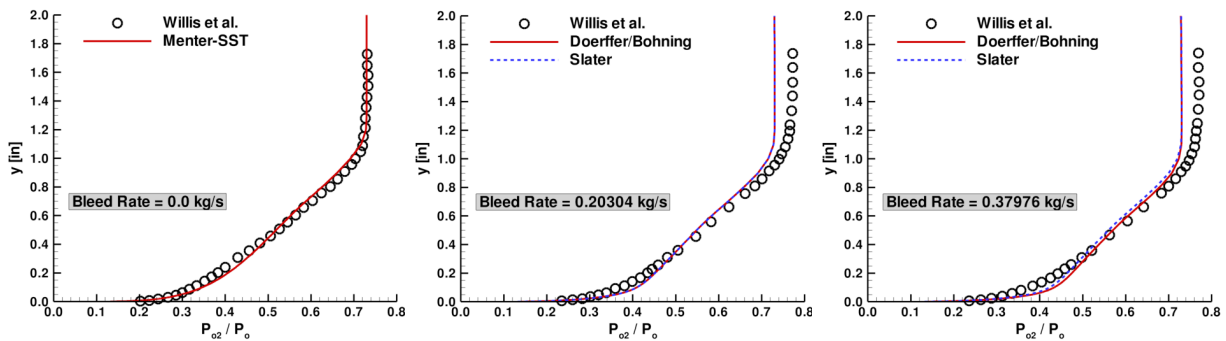


Figure 12: Boundary layer pitot pressure surveys 3.5 inches downstream of the bleed plate (Mach 1.98)

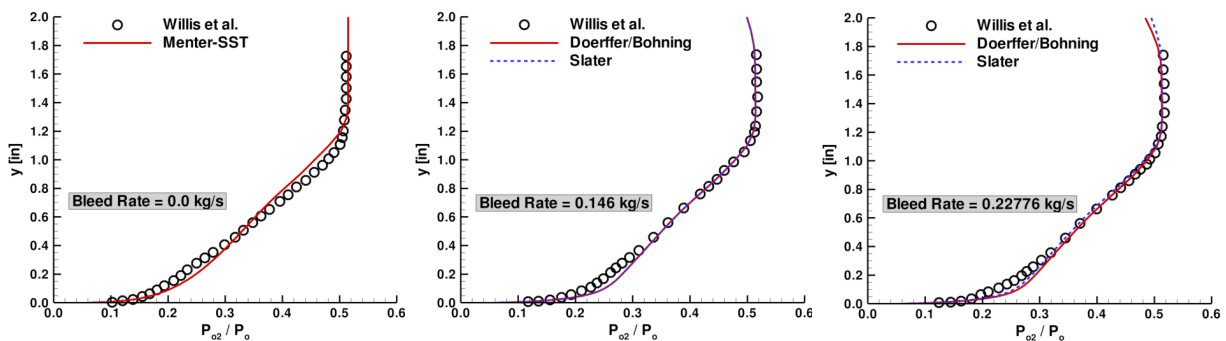


Figure 13: Boundary layer pitot pressure surveys 3.5 inches downstream of the bleed plate (Mach 2.46)

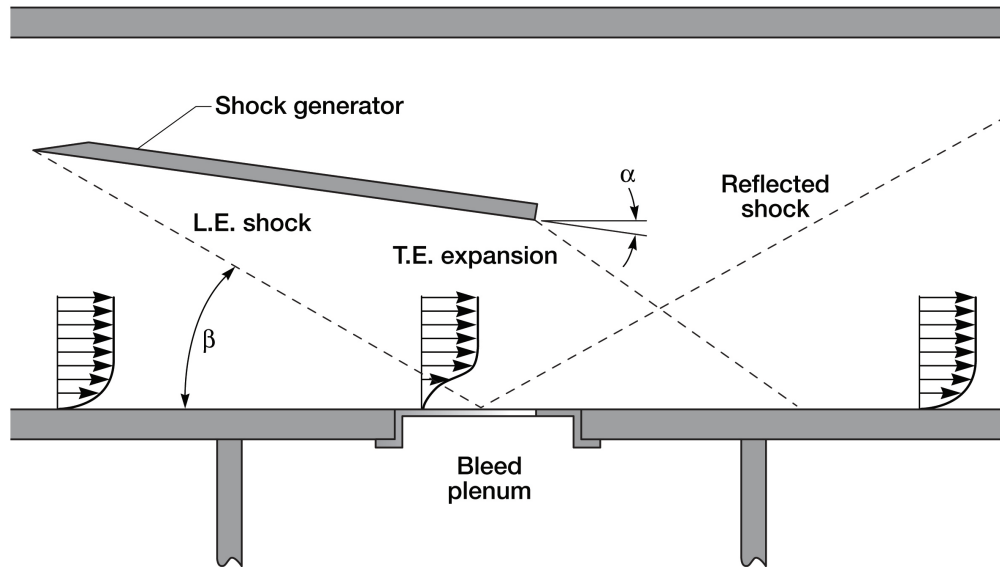


Figure 14: Schematic of the shock impingement on a porous plate tests

grid generated for the three-dimensional simulations included the individual bleed orifices and bleed plenum geometry in the computational domain. These simulations were performed to supplement the experimental data, allowing a more detailed interrogation of the bleed flow physics. The computational domain and grid details are shown in Figs. 15, 16, and 17. The expansion fan emanating from the aft end of the shock generator intersects the tunnel wall at a station that is downstream of the primary region of interest. This allowed some simplifications to be made with regards to how the shock generator geometry was modeled. The first simplification was to simply use a slip wall condition to effectively extend the shock generator horizontally to the outflow plane. Moreover, since the boundary layer on the shock generator was not expected to influence the flow near the porous plate, the entire shock generator surface was treated as a slip wall. This geometric simplification was also used in the simulations performed by Slater.<sup>4</sup> The inflow conditions were set using a flow variable profile extracted from a separate flat plate simulation of sufficient length to allow for the development of a boundary layer that matched the integral properties measured in the experiment. The resulting boundary layer properties extracted from this profile are listed in parentheses along side of the measured values in Table 2. The momentum thickness ( $\theta$ ) was the parameter that was matched precisely, and the resulting percent differences in displacement thickness ( $\delta^*$ ) and skin friction coefficient ( $C_f$ ) were 6.6% and 4.9%, respectively. All flow properties were extrapolated at the outflow and farfield boundaries. The tunnel surface and the interior walls of the bleed orifices were treated as no-slip, adiabatic surfaces. The bleed plenum was modeled as a rectangular domain, with a depth of 16 inches and a length that extended from -8.125 inches to 10.0 inches in the streamwise direction. All of the plenum surfaces were treated as slip walls. For simulations that involved boundary layer bleed, a constant mass flux source term was applied along the lower surface of the plenum. This treatment is analogous to a specified mass flow out boundary condition, with pressure extrapolated from the interior. The porous plate was treated as if it had an infinite span (*i.e.* only a thin slice of the bleed plate was considered), allowing symmetry conditions to be applied at successive bleed columns. One full bleed column and two half columns (12 bleed orifices total) were simulated as shown in Fig. 17.

The grid generated for this geometry consisted of 9,535,488 grid cells distributed over 76 grid blocks (prior to load balancing). The cross-section of each bleed orifice consisted of 1,536 cells distributed using an H-O grid topology. The bleed region consisted of 400 cells distributed in the streamwise direction, resulting in an average streamwise spacing of 0.0375 orifice diameters. The wall-normal grid spacing was set to  $1.0 \times 10^{-4}$  inches, which yielded a nominal  $y^+$  value of 0.21 along the tunnel surface. The grid was stretched away from each no-slip, adiabatic surface at a rate of 7.5%. Excessive grid clustering was avoided in benign

regions of the flow by using topological nesting away from the bleed region as shown in Fig. 16. Finally, the grid generated for the two-dimensional simulations was essentially the symmetry plane extracted from the three-dimensional grid. The two-dimensional grid was only used for simulations that employed the global bleed models, so the facility flow path portion of the flow domain (red section of the grid in Fig. 15) was the only portion of the geometry considered.

The potential benefits of using boundary layer bleed for passive control of shock boundary layer interactions are clearly illustrated in Figs. 18 and 19. Figure 18 shows the Mach contours and streamtraces for flow over the porous plate without boundary layer bleed, and Figure 19 shows the change in the flow field when bleed is applied. The bleed rate chosen for this simulation is half the value that would result in choked flow through the orifices. This amount of bleed reduced the size of the separation substantially, almost to the point of preventing boundary layer separation altogether. The boundary layer downstream of the shock interaction region is also noticeably thinner with higher Mach number values present near the wall. A comparison of the reflected shock systems from both simulations shows that a significant level of shock control can be realized with strategically placed boundary layer bleed systems.

A closer view of the bleed plate region for the simulations with a zero net bleed rate are shown in Figs. 20, 21, and 22 for the three-dimensional, Doerffer/Bohning, and Slater results, respectively. All three simulations show that the flow is recirculating through the porous plate in a clock-wise pattern. This behavior is driven by the pressure gradient induced by the shock boundary layer interaction. In a steady flow, the plenum pressure is constant at some value between the pre- and post- shock pressures. The higher pressure behind the shock locally forces the fluid to bleed into the plenum, while the lower pressure upstream of the shock draws the fluid out of the plenum. This phenomenon can also be visualized in the streamtraces shown in Fig. 18. The Doerffer/Bohning model results predicted a stronger recirculation through the bleed system than predictions obtained from the Slater model. The stronger recirculation pattern results in the overprediction of the separation bubble size (as compared to the three-dimensional CFD results) seen in Fig. 21. It should be noted that the velocity vectors from the three-dimensional simulation, where the bleed fluid is confined to the bleed orifices, are larger than those predicted by the simulations that model the bleed process. The scaling factor between the modeled and the resolved simulation bleed velocity is essentially the porosity of the plate.

A similar set of results are shown in Figs. 23, 24, and 25 for the simulations that considered a net bleed rate that was roughly half of that required to choke the bleed orifices. At this condition, all three simulations are still showing signs of flow recirculation through the bleed plate, although most of the bleed ports are forcing the flow into the plenum. At this condition, the Doerffer/Bohning model is still predicting a stronger recirculation than the results obtained from the Slater model. The results obtained from the Slater model show the boundary layer is now completely attached at this bleed condition, while the Doerffer/Bohning model results show that a small amount of boundary layer separation is still present (due to the stronger bleed recirculation pattern), which is consistent with the three-dimensional CFD simulation results. Although not shown, at the maximum bleed flow rate (*i.e.* the flow rate that chokes the bleed system) all of the bleed passages are bleeding flow from the boundary layer into the plenum.

The computational results are compared with the measured centerline surface pressure distribution (normalized by the approach flow pressure,  $P_1$ ) in Fig. 26. The top image compares the measured baseline pressures (where the bleed holes have been filled in) and zero net bleed flow rate pressures (where the bleed holes are not filled in) to the computational results. Focusing first on the two sets of measured pressures, it is noted that the pressure distribution through the bleed region is slightly altered depending on whether the bleed holes are covered. The pressure distribution through the bleed region is somewhat closer to the theoretical inviscid distribution when the bleed holes are covered (baseline condition). When the bleed orifices are left open, the pressure distribution rises more sharply near the beginning of the bleed region and flattens out near the end of the bleed region. This behavior is a result of the flow recirculation pattern that was discussed previously. The effusion of fluid from the plenum near the beginning of the bleed region tends to increase the height of the recirculation zone, locally inducing a somewhat stronger separation shock. Towards the end of the bleed region, the bleeding of fluid into the plenum acts to locally decrease the size of the separation bubble, reducing the rate of compression. The non-monotonic rise in

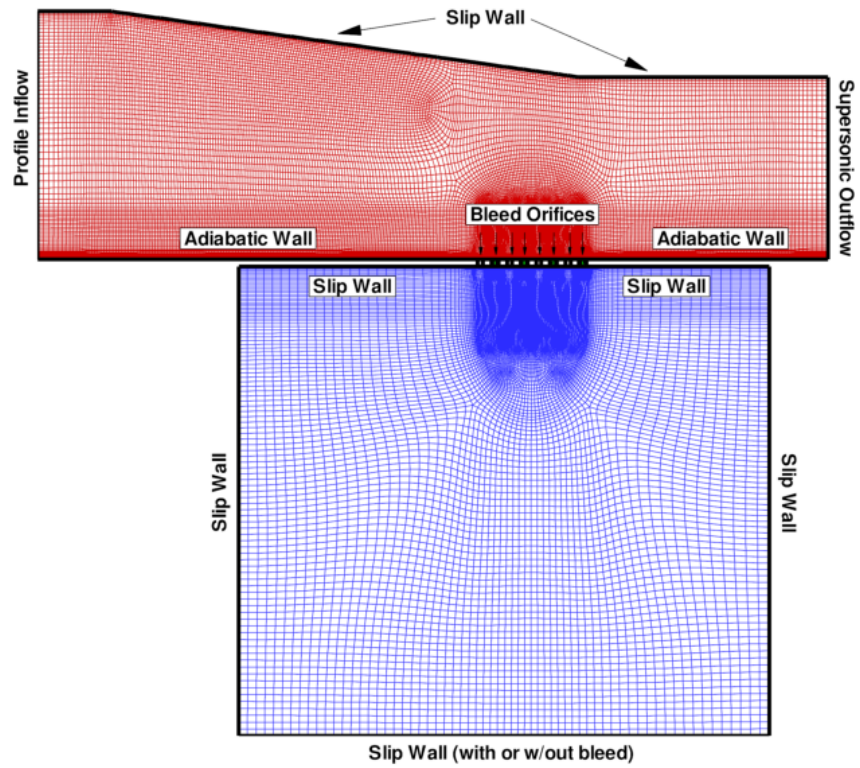


Figure 15: Solution domain for the 3-D oblique shock porous plate (every other point removed)

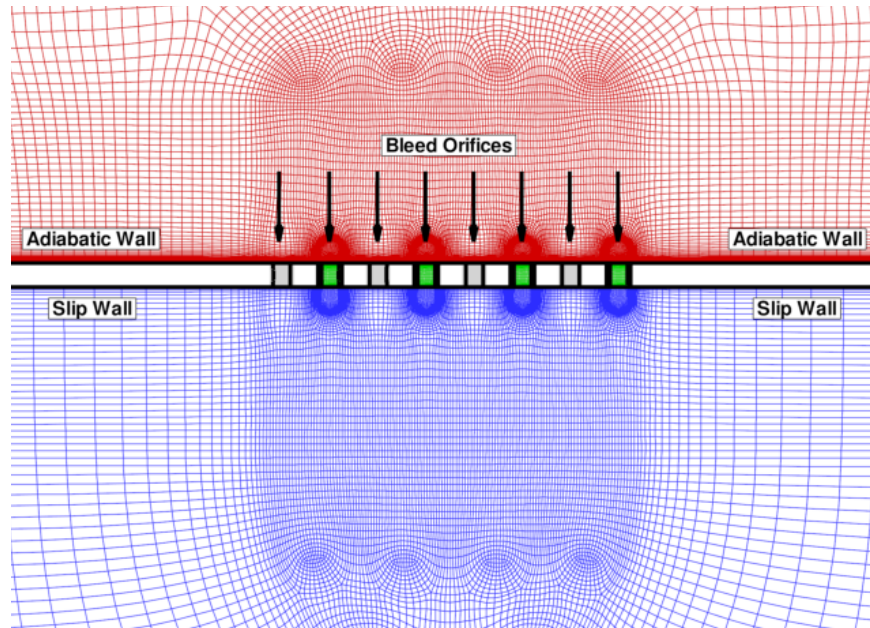


Figure 16: Nearfield of bleed region for the 3-D oblique shock porous plate (every other point removed)

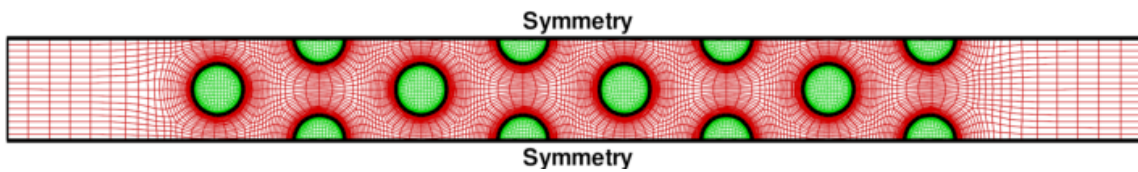


Figure 17: Wall-normal view of the bleed orifices (every other point removed)

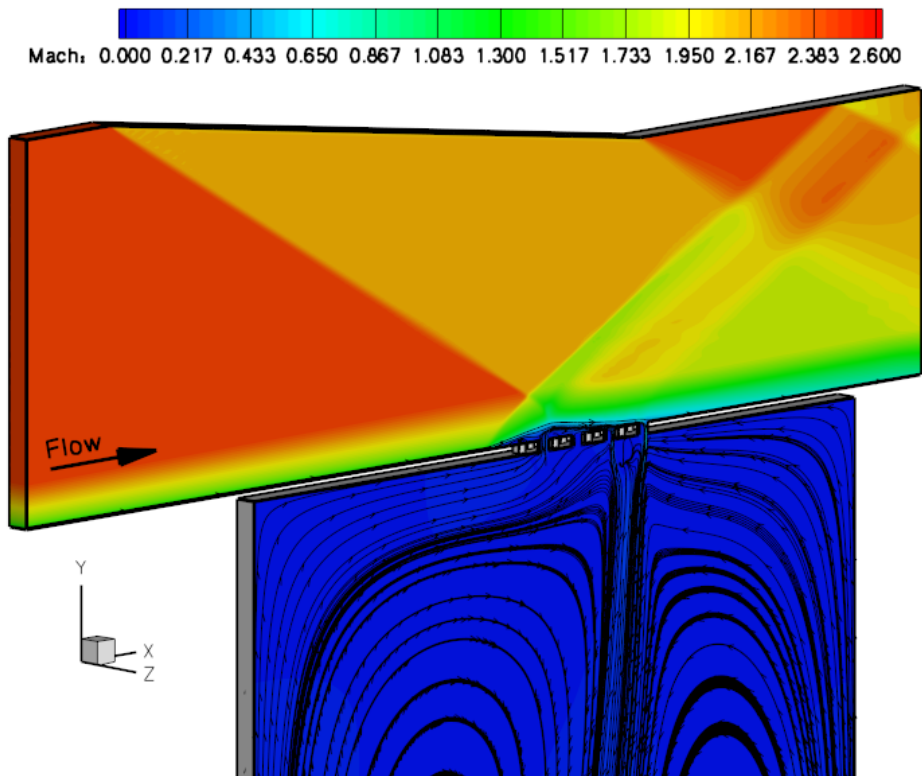


Figure 18: Mach contours and streamtraces for  $\dot{m}_{bleed} = 0.0$  kg/s

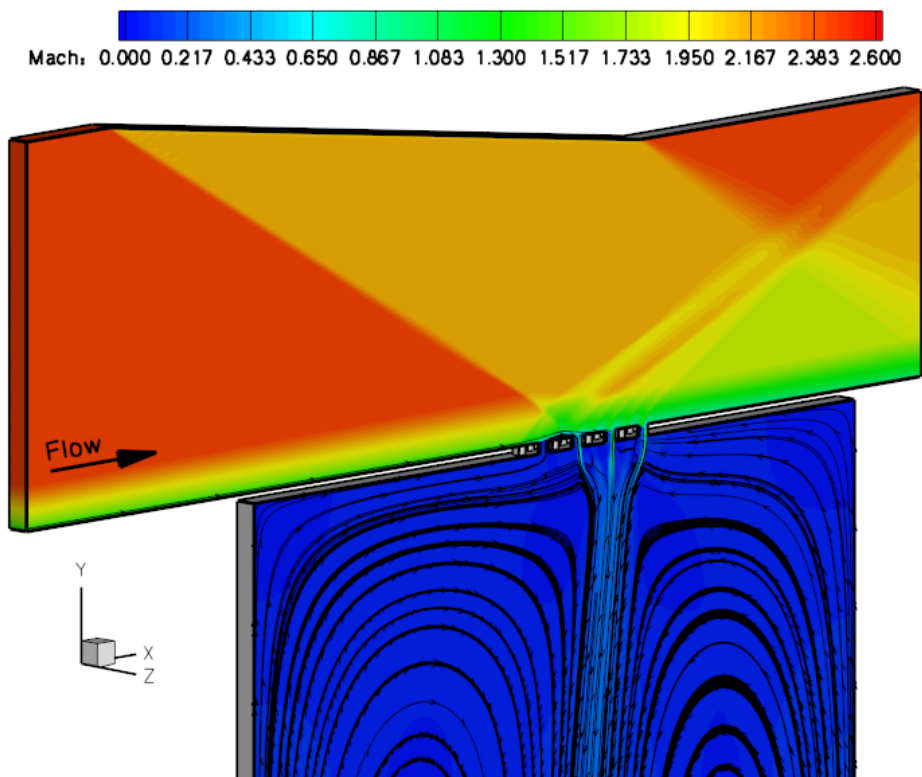


Figure 19: Mach contours and streamtraces for  $\dot{m}_{bleed} = 3.1875 \times 10^{-3}$  kg/s

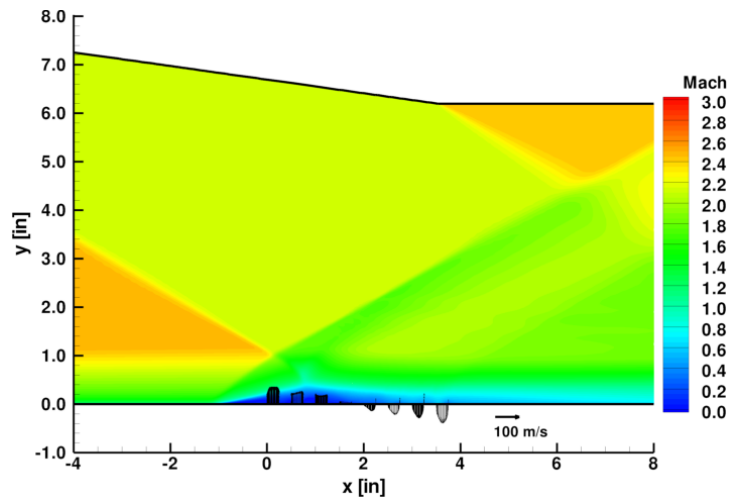


Figure 20: Mach contours and bleed velocity vectors for zero net bleed (resolved orifices)

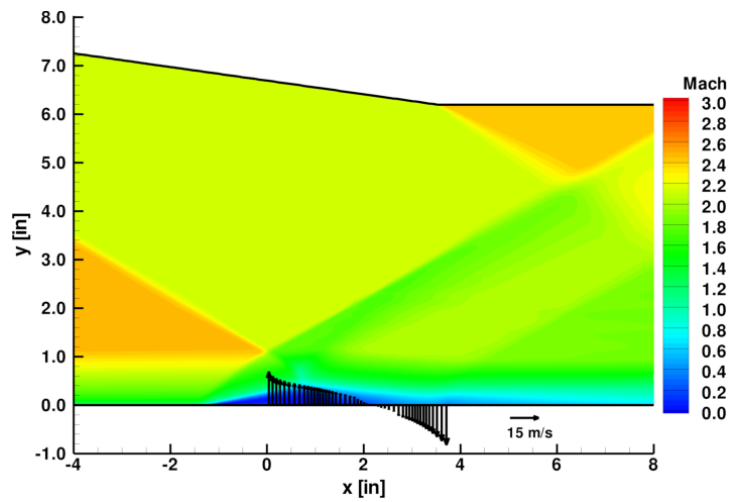


Figure 21: Mach contours and bleed velocity vectors for zero net bleed (Doerffer/Bohning)

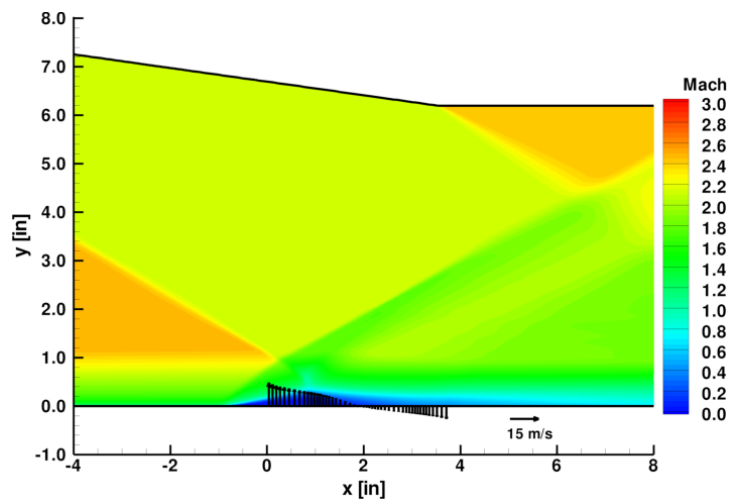


Figure 22: Mach contours and bleed velocity vectors for zero net bleed (Slater)

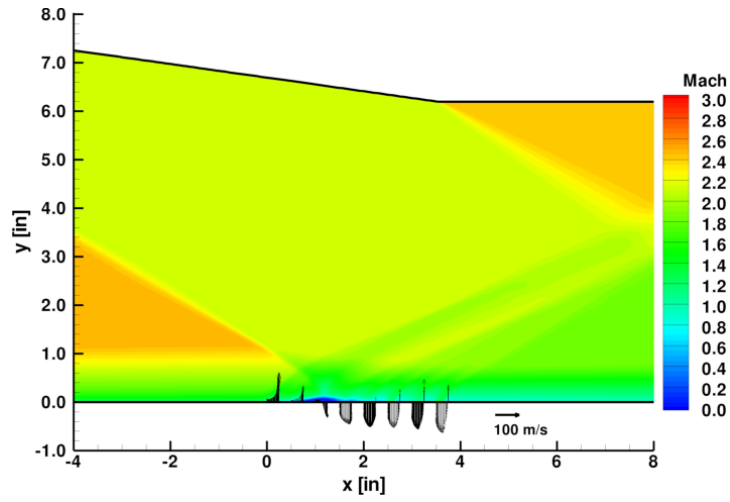


Figure 23: Mach contours and bleed velocity vectors for bleed at half the choking limit (resolved orifices)

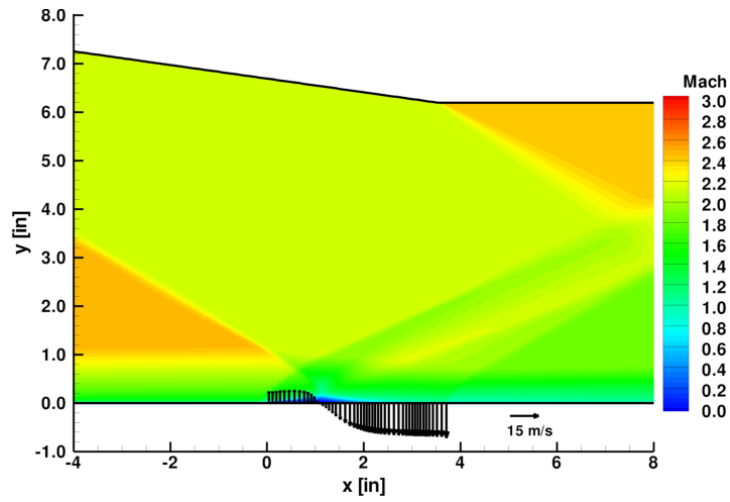


Figure 24: Mach contours and bleed velocity vectors for bleed at half the choking limit (Doerffer/Bohning)

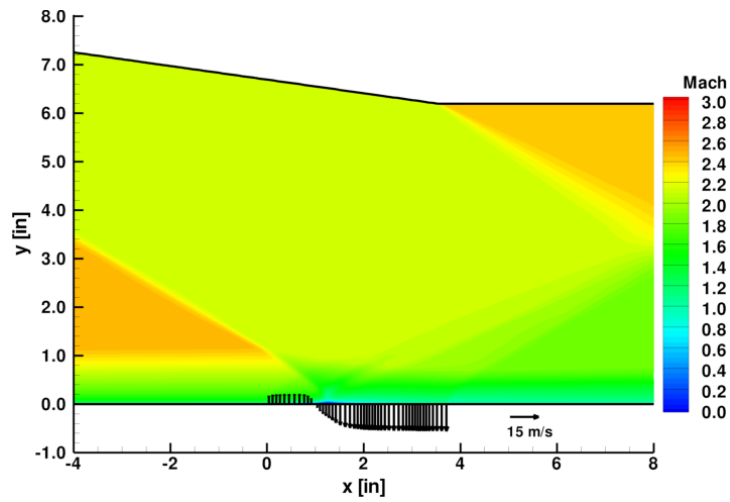


Figure 25: Mach contours and bleed velocity vectors for bleed at half the choking limit (Slater)

pressure through the bleed region displayed in the three-dimensional CFD data is a result of local compressions and expansions as the flow negotiates around the bleed orifices. The experimental pressure taps are too far apart to pick this phenomenon up.

The center image of Fig. 26 compares the measured surface pressure distribution to the computed values when the bleed mass flow rate was half that required to choke the porous bleed openings. At this condition, the measurements and all three simulations are still showing signs of flow recirculation through the bleed system. The localized expansions and compressions seen in the three-dimensional CFD results are stronger at this condition due to the additional turning of the flow as it is bled into the plenum. The measurements are also beginning to show some signs of non-monotonic behavior near the last 4 pressure taps of the porous region (between the  $x \approx 2.75$  and  $x \approx 3.75$  inch stations). The amount of boundary layer separation exhibited by the Slater model was smaller than the Bohning model results and three-dimensional CFD results at this bleed condition (see Figs. 23, 24, and 25), which explains the smaller initial pressure rise at the start of the bleed region. As the bleed rate approaches its choking limit (bottom image of Fig. 26), all of the bleed ports are bleeding boundary layer fluid into the plenum, as indicated by the initial expansion present at the start of the bleed region seen in the measurements and each of the CFD solutions. The three-dimensional CFD results show that the localized expansions and compressions have gotten even stronger, and the measured results are now clearly indicating the same phenomenon. As a final note, the pressure drop that occurs downstream of the  $x \approx 10$  inch station is a result of the expansion fan formed at the trailing edge of the shock generator. Due to the approximations made in modeling the shock generator, the comparisons with measurements should not be attempted downstream of this station. The pressure rise just upstream of this pressure drop (seen in the measurements) was not captured in the CFD simulations. This pressure rise was conjectured to be the result of flow spillage over the boundary layer fences in Ref. 11, but there was no data gathered to support or rebut this claim.

Comparisons of the boundary layer pitot pressure profiles with measurements are shown in Figs. 28, 29, and 30. The purple dashed line in each of these images denotes the boundary layer thickness of the approach stream. The image on the left of each of these figures contains the pitot pressure profile at the reference plane  $x = -3.225$  inches, which was reported in Ref. 11 to be independent of the bleed rate considered. However, the measured profiles for the boundary layer at this station show a slight variation with and without the presence of boundary layer bleed. The profiles extracted from the CFD simulations agree more closely with the upstream profiles when non-zero bleed rates were considered. The center image shows the pitot pressure profiles extracted at a station just downstream of the porous region of the plate. The overall level of agreement with the measurements within the boundary layer at this station is favorable for each of the computational models for the zero net bleed condition, but the wave structure near the boundary layer edge is not predicted well by any of the computational models. As the bleed rate is increased, the bleed models tend to somewhat overpredict the impact of bleed on the pitot profiles. The three-dimensional CFD results compare well with the measurements for each bleed flow rate at this station. Further downstream, the boundary layer starts to recover towards a pseudo-equilibrium state, and all of the computational models are reproducing the experimental results to a reasonable degree of accuracy.

Calculations were repeated on coarse grids for both the three-dimensional and two-dimensional modeling approaches to ensure that the numerical (truncation) errors were acceptably small. For the purposes of this effort, an acceptably small numerical error is a value that is much less than the differences noted between solutions obtained from the use of the different bleed models. The condition chosen for this evaluation was the bleed mass flow rate that corresponded to half the value required to choke the bleed system. Based on the comparisons above, the centerline surface pressure showed the most sensitivity between the models, so this quantity was the focal point of the error analysis. Every other grid point was removed from the fine grid to create the coarse grids (*i.e.* full coarsening was performed). A comparison of the centerline wall pressures for each grid are shown in Fig 31. As is evident in this plot, the solutions for each grid system are practically identical. The average percent differences between the centerline pressures on each grid system were 0.12%, 0.11%, and 0.21% for the Doerffer/Bohning model, Slater model, and three-dimensional resolved bleed orifice simulations, respectively.

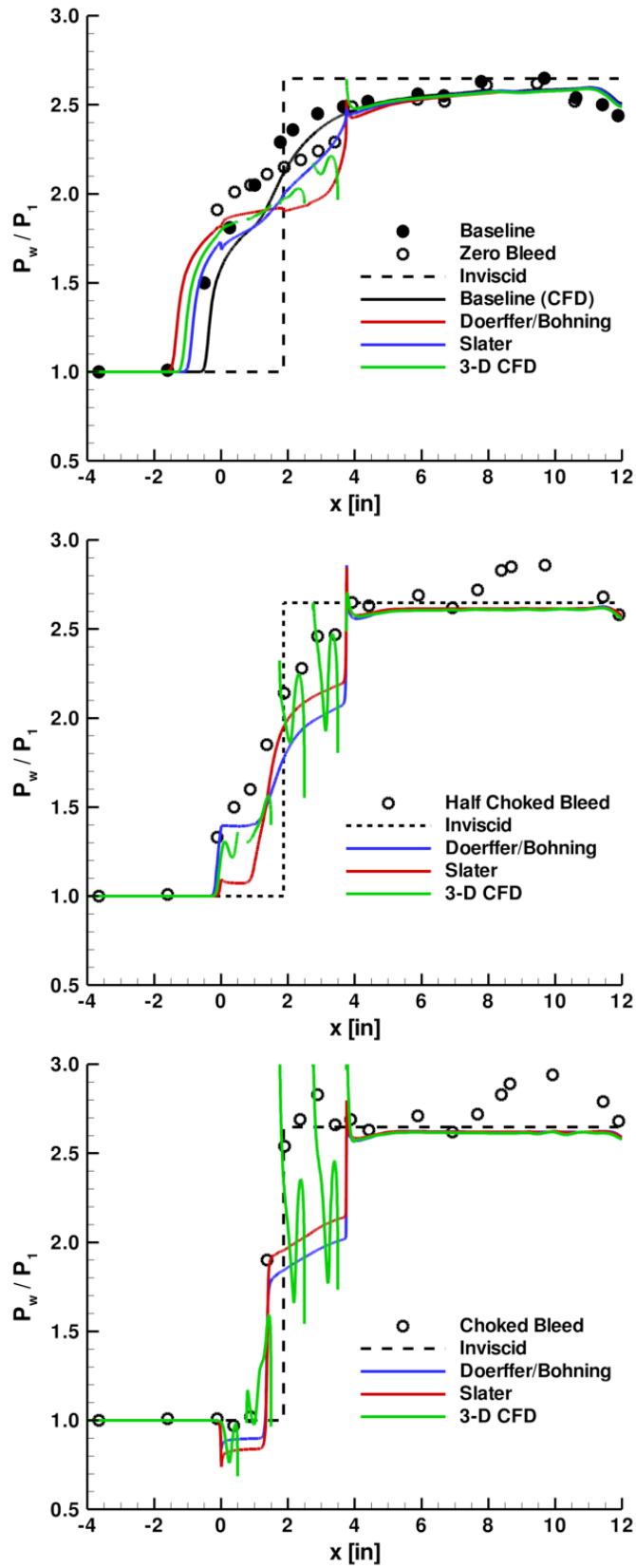


Figure 26: Wall pressure distributions with varying bleed flow rates

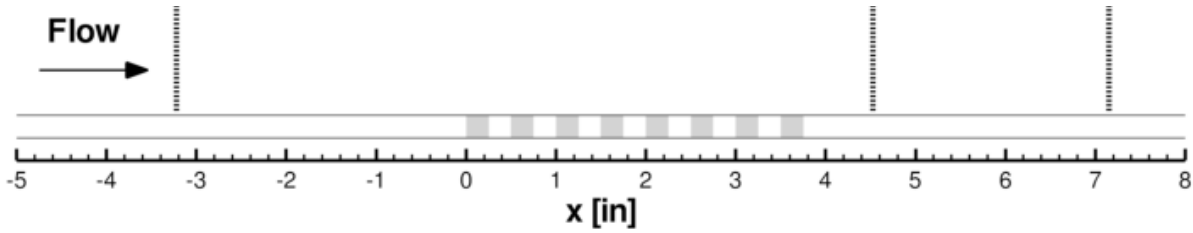


Figure 27: Schematic of pitot pressure profile stations along the porous plate

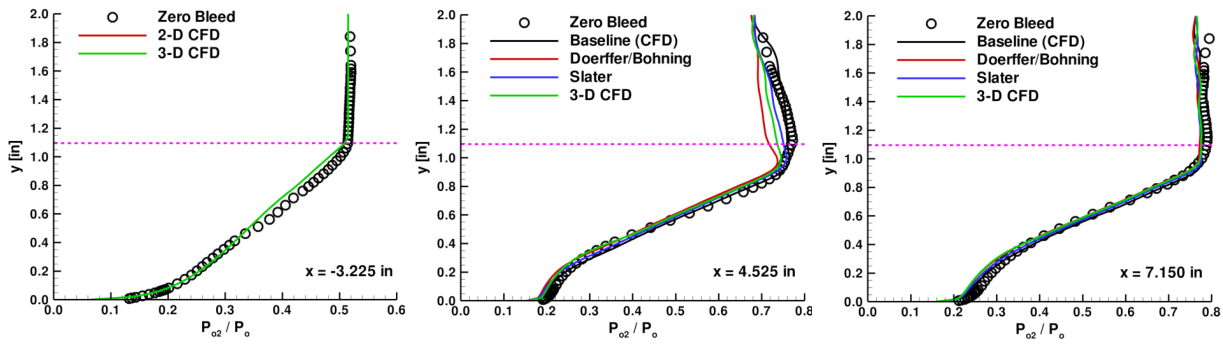


Figure 28: Boundary layer pitot pressure surveys without bleed

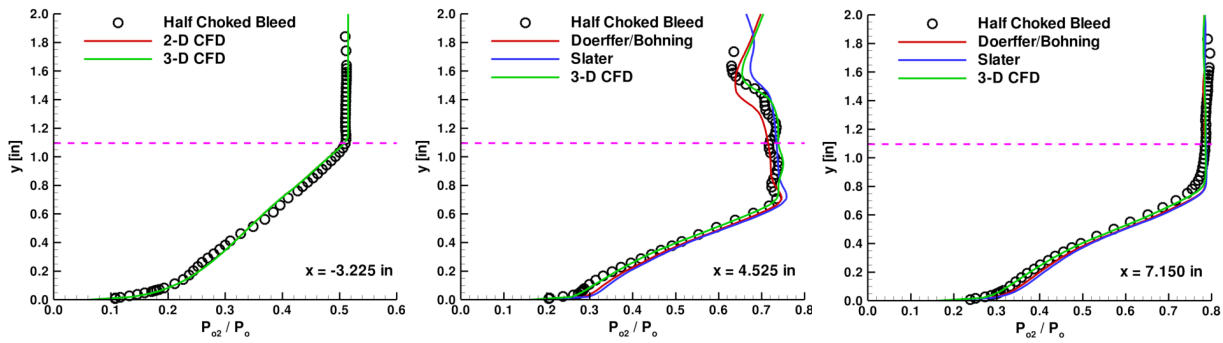


Figure 29: Boundary layer pitot pressure surveys with half of the choked bleed flow rate

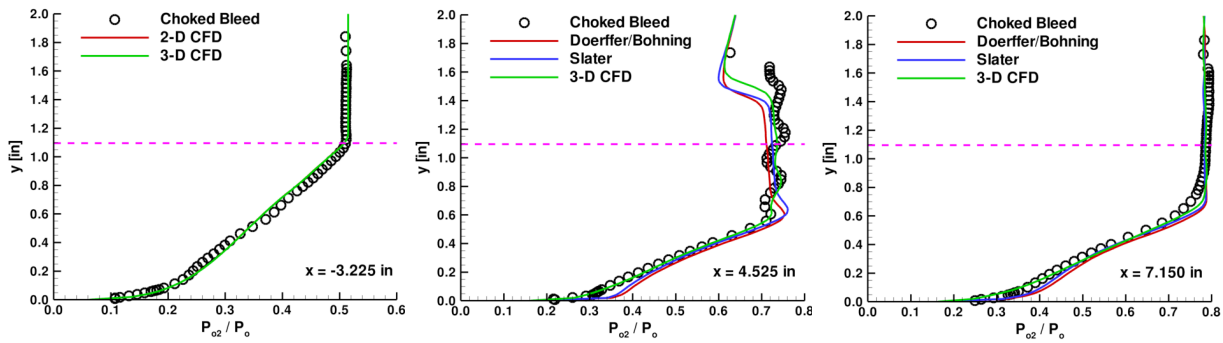


Figure 30: Boundary layer pitot pressure surveys with choked bleed flow rate

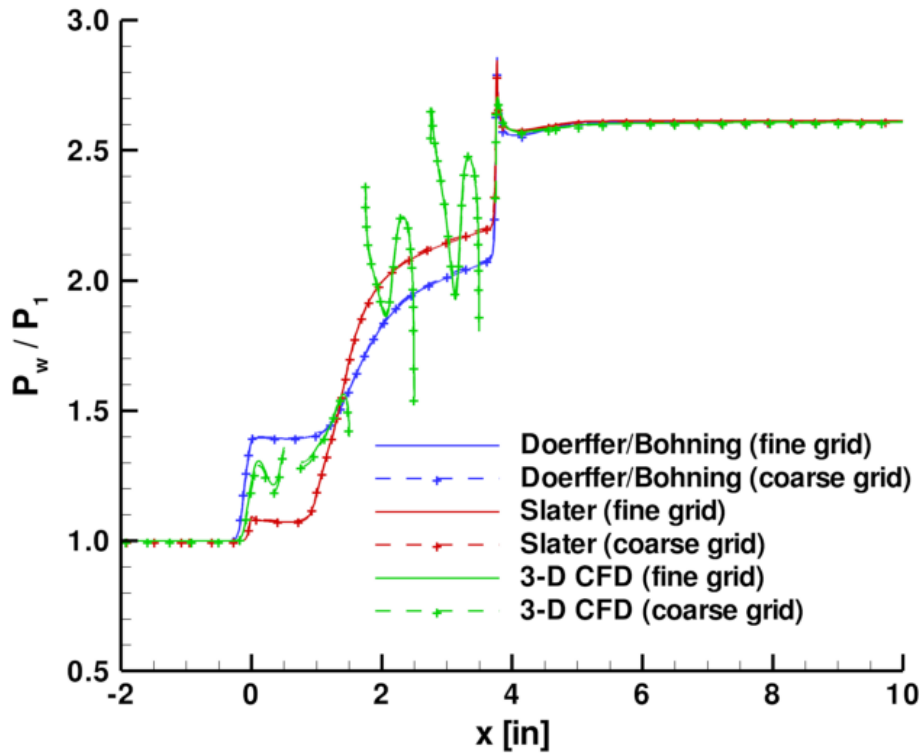


Figure 31: Effect of grid resolution on centerline wall pressure (half choked bleed rate condition)

## SUMMARY

A boundary layer effusion modeling framework has been developed to allow for the modeling of geometrically complicated bleed systems without requiring the tedious set up and costly simulation time associated with a direct simulation of the detailed bleed system. The present framework is based on the use of source (or sink) terms in lieu of the common practice of specifying the bleed process directly as a boundary condition. This framework offers some advantages over standard approaches based on the setting of a transpiration boundary condition:

- The wall boundary condition can remain unchanged, a reasonable approach given that the porosity of practical bleed systems is typically  $\ll 1$ .
- The specification of source terms offers a direct path to add empirical models for  $2^{nd}$ -order effects that may be difficult to account for by simply applying “effective” transpiration values as a boundary condition.
- Concerns about the “well-posedness” of the boundary condition may be alleviated.

The Doerffer/Bohning and the Slater effusion models, both of which were specifically tailored for supersonic flows, have been implemented into this framework. Both effusion models were tested against unit problems that contain key aspects of the flow physics applicable to bleed systems tailored for hypersonic air-breathing propulsion systems. In particular, supersonic flows over a porous plate were simulated (with and without the presence of shocks) for a range of bleed flow rates. In general, both of the effusion formulations qualitatively induced the proper response of the boundary layer as it passed through and downstream of the porous bleed systems considered in this study. Even in the presence of shock waves, both formulations

did a more than adequate job of reproducing the observations seen in the measurements and the three-dimensional simulations that directly resolved the bleed system. A larger sample of test cases, however, is required to fully validate the formulations. This is particularly necessary for the Slater model, since most of the measurements used to compare the models against were the same data used to formulate this model.

## ACKNOWLEDGMENTS

This effort was funded through the Hypersonics Project (Propulsion Discipline) of the Fundamental Aerodynamics Program and carried out at the Hypersonic Airbreathing Propulsion Branch of the NASA Langley Research Center. The authors would like to express their sincere gratitude to John Slater and David Davis from the Inlet and Nozzle Branch at the NASA Glenn Research Center for several helpful discussions and for providing files for most of the experimental data utilized in this effort.

## REFERENCES

- [1] Bur, R., ***Passive Control of a Shock Wave/Turbulent Boundary Layer Interaction in a Transonic Flow***, Tech. Rep. 1992-6 (Nov.-Dec. 1992).
- [2] Poll, D. I. A., Danks, M., and Humphreys, B. E., ***The Aerodynamic Performance of Laser Drilled Sheets***, in *Proc. of the 1st European Forum on Laminar Flow Technology, Hamburg*, pages 274–277 (March 1992).
- [3] Doerffer, P. P. and Bohning, R., ***Modelling of Perforated Plate Aerodynamics Performance***, Tech. Rep. 8 (Nov. 2000).
- [4] Slater, J. W., ***Improvements in Modeling 90-degree Bleed Holes for Supersonic Inlets***, AIAA Paper 2009-0710 (Jan. 2009).
- [5] Willis, B. P., Davis, D. O., and Hingst, W. R., ***Flow Coefficient Behavior for Boundary Layer Bleed Holes and Slots***, AIAA Paper 1995-0031 (Jan. 1995).
- [6] VULCAN, <http://vulcan-cfd.larc.nasa.gov/> (April 2011).
- [7] Edwards, J. R., ***A Low Diffusion Flux-Splitting Scheme for Navier-Stokes Calculations***, *Computers & Fluids*, 26(6):635–659 (1997).
- [8] van Leer, B., ***Towards the Ultimate Conservation Difference Scheme. II. Monotonicity and Conservation Combined in a Second Order Scheme***, *Journal of Computational Physics*, 14:361–370 (1974).
- [9] Menter, F. R., ***Zonal Two Equation  $k-\omega$  Models for Aerodynamic Flows***, AIAA Paper 93-2906 (July 1993).
- [10] Willis, B. P. and Davis, D. O., ***Boundary Layer Development Downstream of a Bleed Mass Flow Removal Region***, AIAA Paper 1996-3278 (July 1996).
- [11] Willis, B. P., Davis, D. O., and Hingst, W. R., ***Flowfield Measurements in a Normal-Hole-Bled Oblique Shock-Wave and Turbulent Boundary-Layer Interaction***, AIAA Paper 1995-2885 (July 1995).